



AIAA 2002-2917

**Nonintrusive Temperature and
Velocity Measurements in a
Hypersonic Nozzle Flow**

S. O'Byrne , P.M. Danehy

NASA Langley Research Center, Hampton, VA 23681

and A.F.P. Houwing

Australian National University, Canberra, Australia 0200

**22nd AIAA Aerodynamic Measurement
Technology and Ground Testing Conference
June 24–26, 2002 / St Louis, MI**

Nonintrusive Temperature and Velocity Measurements in a Hypersonic Nozzle Flow

S. O'Byrne*, P.M. Danehy†

NASA Langley Research Center, Hampton, VA 23681

and A.F.P. Houwing‡

Australian National University, Canberra, Australia 0200

Distributions of nitric oxide vibrational temperature, rotational temperature and velocity have been measured in the hypersonic freestream at the exit of a conical nozzle, using planar laser-induced fluorescence. Particular attention has been devoted to reducing the major sources of systematic error that can affect fluorescence temperature measurements, including beam attenuation, transition saturation effects, laser mode fluctuations and transition choice. Visualization experiments have been performed to improve the uniformity of the nozzle flow. Comparisons of measured quantities with a simple one-dimensional computation are made, showing good agreement between measurements and theory given the uncertainty of the nozzle reservoir conditions and the vibrational relaxation rate.

Nomenclature

B	Einstein B coefficient for stimulated absorption/emission, cm J^{-1}
e_{vib}	Vibrational energy, J
E	Laser energy, J
F	Transition rotational energy, cm^{-1}
G	Transition vibrational energy, cm^{-1}
I	Laser irradiance, W cm^{-2}
J	Rotational quantum number
k	Boltzmann constant, $\text{K}^{-1} \text{cm}^{-1}$
l_{flow}	Flow length scale, m
R	Specific gas constant, $\text{J kg}^{-1} \text{K}^{-1}$
Sig	Fluorescence signal intensity, photons Sr^{-1}
T	Rotational temperature, K
u	Velocity x -component, m s^{-1}
x	Axial distance, m
Θ_{vib}	Characteristic temperature, K
τ_{vib}	Characteristic V-T relaxation time, s

Introduction

FREE-PISTON shock tunnels have proved to be effective ground-test facilities for investigating the effects of high-velocity flight on vehicles. One obstacle to the use of these facilities for explaining the physics of hypersonic flight is that the flow generated by a

shock tunnel differs fundamentally from the air flow encountered by a vehicle moving through air at hypersonic speed. The acceleration of the test gas in a shock tunnel is generated by the expansion of shock-compressed gas which is in high-temperature thermal equilibrium in the nozzle reservoir. As the flow in the nozzle expands, the rapid decrease in pressure can lead to thermal and/or chemical freezing,¹ where the collision rate is insufficient for the chemical or vibrational energy to achieve equilibrium but sufficiently rapid to allow the rotational and translational energy components to reach their equilibrium values.

This vibrational or chemical nonequilibrium condition implies that the flow generated by these facilities contains more thermal energy than the flow of equilibrium air with the same rotational temperature. The excess energy is liberated when the molecular collision rate becomes sufficiently high, for example downstream of the bow-shock generated by a body. This extra energy then generates a greater increase in rotational temperature across the shock layer and more surface heat-flux than expected from a comparable equilibrium flow. Lack of quality measurements of this excess energy may cause its effects to be poorly estimated or ignored, sometimes leading to large discrepancies between measurements and calculations.

It is especially difficult to completely model the vibrational freezing of molecular species in nozzle flows. The vibration-translation (V-T) relaxation processes are usually modeled using a simplified Landau-Teller mechanism.^{2,3} This model assumes the molecules behave as harmonic oscillators, and this may not be the case for the sudden expansions in nozzle flows. The model also uses characteristic relaxation times determined empirically by measuring relaxation distances behind shock waves,^{4,5} often at temperatures well

*NRC Postdoctoral Fellow, Hypersonic Airbreathing Propulsion Branch, MS168. AIAA member.

†Research Scientist, Instrumentation Systems Development Branch MS 236. AIAA member.

‡Reader, Department of Physics and Theoretical Physics. AIAA member.

Copyright © 2002 by the American Institute of Aeronautics and Astronautics, Inc. No copyright is asserted in the United States under Title 17, U.S. Code. The U.S. Government has a royalty-free license to exercise all rights under the copyright claimed herein for Governmental Purposes. All other rights are reserved by the copyright owner.

above those of expanding nozzle flows. The validity of these approximations has been a subject of intense experimental and theoretical scrutiny, as the processes of excitation behind a shock wave and de-excitation in an expanding nozzle flow may involve different physical processes. Recent experimental investigations in nitrogen and air flows⁶⁻⁹ tend to support the validity of the Landau-Teller V-T mechanism for expanding nozzle flows, at least to a first approximation. Earlier results indicating much faster relaxation rates¹⁰ have since been attributed to the presence of impurities in the flow. Calculations indicate that impurities such as water¹¹ or metal contaminants¹² from the tunnel walls significantly enhance the relaxation of molecular species in nozzle flows.

Planar laser-induced fluorescence (PLIF) of nitric oxide (NO) is used for the measurements presented here. It is well established as a versatile diagnostic technique and has been used to measure rotational temperature,¹³⁻¹⁵ velocity,¹⁶ and pressure.¹⁷ Palmer and Hanson¹⁸ measured rotational and vibrational temperature in a supersonic nozzle flow using NO PLIF. This measurement showed vibrational freezing of the NO molecules.

Most relevant to this investigation is the work of Palma et al.,¹⁹ in which NO PLIF was used to measure vibrational and rotational temperatures in the same facility as these measurements, at a different freestream condition. Palma et al. measured rotational temperatures in good agreement with calculations but the measured vibrational temperatures, although they showed frozen vibrational behavior, did not agree with the calculation. This disagreement was attributed to nonlinearities in the imaging system and nonuniformity in the flow assumed to be due to contamination by driver gas. In an effort to minimize these uncertainties in the freestream flow properties of this facility, the present paper describes experiments performed to accurately determine the velocity, rotational temperature and NO vibrational temperature at the nozzle exit of a free-piston shock tunnel using PLIF.

This paper begins with a discussion of the T2 free-piston shock tunnel facility²⁰ in which the experiments were performed, the method of calculating the nominal freestream conditions and the pitot- pressure measurements used to account for the nozzle boundary layer. PLIF visualization experiments are used to determine the cause and solution of nonuniformity in the nozzle flow. The theory underlying NO PLIF thermometry is then summarized, emphasizing those aspects of PLIF measurements that have to be minimized to ensure minimal systematic error. Finally, nozzle-exit rotational temperature, NO vibrational temperature and velocity distributions are presented and compared to the predictions of a one-dimensional nozzle calculation. This investigation formed part of a more extensive investigation of hypersonic viscous flows.²¹

The T2 Facility

The T2 free-piston shock tunnel facility has been in continual use since 1966, and can generate flows with stagnation enthalpies between 3 and 21 MJ kg⁻¹. Although it has a shorter flow duration and smaller test section than subsequent free-piston shock tunnels, this facility is well suited to the development of new diagnostic techniques, particularly those that require a large number of tunnel runs for a good measurement. The T2 facility has a much shorter turnaround time and is much less expensive to run than larger facilities. The small test section is particularly advantageous for laser-induced fluorescence measurements because it makes the facility less prone to systematic errors caused by attenuation of the laser sheet as it propagates through the flow.

Figure 1 shows the main components of the T2 facility. The free-piston shock tunnel is a combination of a shock tube and a hypersonic nozzle. This facility produces high shock speeds by using a free-piston driver. The piston reservoir, shown at the left of Figure 1, is filled with air to a predetermined pressure (4.3 MPa in the case of the present experiments), at which time the piston is released. The piston is then accelerated by the expanding high-pressure gas and, in turn, adiabatically compresses the driver gas – typically helium or a mixture of helium and argon. These gases are chosen because they will not lose energy through chemical reactions at the high temperatures in the test gas and because the low molecular weight of helium allows very high shock speeds to be attained in the shock tube, due to the increased sound speed for a gas with low molecular weight.²² Filling pressures for the driver and test gases are included in Table 1.

Once the piston has compressed the driver gas sufficiently, the mild steel diaphragm dividing the driver gas in the compression tube from the test gas in the shock tube bursts. The pressure of the driver gas is initially much higher than the pressure of the test gas, so a shock wave propagates along the shock tube. The shock wave heats and compresses the test gas and is reflected from the end-wall of the shock tube, once again heating and compressing the test gas. Upon shock reflection the hot, high-pressure test gas bursts the diaphragm in the nozzle throat and expands through a conical converging-diverging nozzle. The nozzle has a 7.5° half-angle, a 7-mm throat diameter, is 259 mm long and has an exit-to-throat area ratio of 110.6.

The nozzle design and the large initial pressure difference between conditions in the nozzle reservoir and at the nozzle exit – which is evacuated to approximately 20 Pa prior to the tunnel run – ensure that a hypersonic flow is generated at the nozzle exit. After passing over the model, the test gas empties into the dump tank. At these conditions, steady test conditions last approximately 300 μ s before driver gas contaminates the test flow.

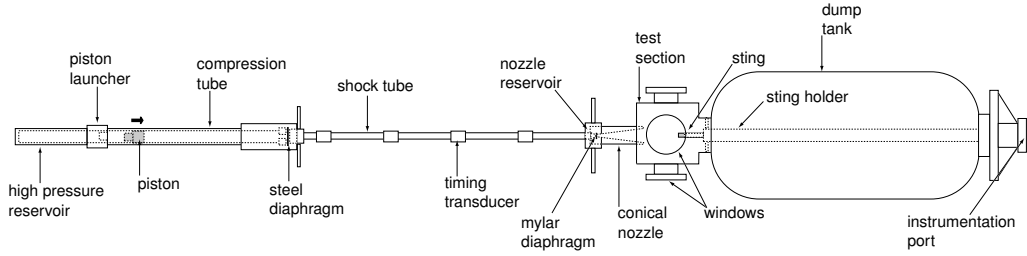


Fig. 1 The T2 free-piston shock tunnel facility.

Computed Flow Conditions

The ESTC code²³ is used to calculate the nozzle-reservoir temperature (and hence the stagnation enthalpy), based on the shock speed and nozzle-reservoir temperature measured by a pair of pressure transducers in the shock tube. ESTC solves the one-dimensional shock tube equation²² for a reflected shock with initial speed given by the measured shock speed. The calculated nozzle-reservoir pressure is then compared to the measured nozzle-reservoir pressure, and the flow conditions are isentropically expanded or compressed until the computed reservoir pressure matches the measured pressure. In this way, the code goes some way toward accounting for the losses in the facility. ESTC does not account explicitly for phenomena such as shock-speed attenuation due to viscosity, energy loss by radiation and conduction to the shock tube walls or cooling caused by the mixing of cooler driver gas with the test gas. The isentropic correction of the calculated pressure to the measured pressure partially compensates for these losses.

The conditions at the nozzle exit are calculated using the STUBE code.²⁴ This nozzle code was specifically designed to determine free-piston shock tunnel freestream conditions. The code assumes one-dimensional, inviscid nozzle flow, but accounts for chemical nonequilibrium using a 10-species reaction mechanism. It accepts as inputs the geometry of the flow, the chemical composition of the test gas, the measured nozzle-reservoir pressure and the nozzle-reservoir temperature as calculated by ESTC. These quantities are used to determine the chemical composition and the state variables of the nozzle flow as a function of axial distance.

STUBE has been modified to account for vibrational nonequilibrium using a sudden-freezing approximation based upon that put forward in Ref. 1. Assuming an equilibrium Boltzmann distribution, the vibrational energy of each species is given by³

$$e_{vib} = \frac{\Theta_{vib}}{\exp(\Theta_{vib}/T) - 1} R \quad (1)$$

where Θ_{vib} is a characteristic vibrational temperature for the species and R is the specific gas constant. An initial calculation assuming vibrational equilibrium is performed, and the rate of change of vibrational energy of each species is used to determine a characteristic

flow length scale, l_{flow} , defined using

$$l_{flow} = \frac{e_{vib}}{de_{vib}/dx} \quad (2)$$

This flow length scale is directly compared with another length scale dictated by the vibrational relaxation rate at the local temperature and pressure conditions. This rate is calculated by STUBE using the Landau-Teller model for V-T relaxation time:

$$\tau_{vib} = C \frac{\exp \left[(K/T)^{\frac{1}{3}} \right]}{p} \quad (3)$$

The constants C and K are taken from Ref. 3. The vibrational length scale l_{vib} is given by the product of the local flow velocity and τ_{vib} . As the calculation proceeds along the nozzle, the value of $\log(l_{flow}/l_{vib})$ is monitored at each x position. The molecular species is deemed to be frozen at the temperature for which this ratio becomes negative. The code is then set to ensure freezing for this species and the calculation recommenced until the freezing temperature of the next species is reached. The sequence of steps is repeated for N₂, O₂ and NO freezing temperatures.

Pitot Survey

The boundary-layer displacement thickness in the nozzle reduces the effective flow divergence angle, an effect that is not accounted for in the inviscid STUBE calculation. The displacement caused by the boundary layer was determined using an axial pitot-pressure survey at four locations, extending upstream and downstream of the nozzle exit. The pitot pressure was measured using a PCB brand piezoelectric transducer mounted in a cylindrical brass housing. The effective divergence angle of the nozzle was changed in the STUBE calculation until the measured and calculated pitot pressure measurements agreed, as shown in Fig. 2. Here the axial distance is plotted relative to the nozzle exit. The best fit to the data for the fluid inside the nozzle was achieved using a divergence half-angle of $6.8 \pm 0.3^\circ$.

Once the correct nozzle divergence angle was ascertained, the freestream properties were calculated as a function of axial distance. The nozzle-exit conditions are summarized in Table 1. A 99% N₂, 1% O₂ mixture was chosen for the shock tube fill condition. The

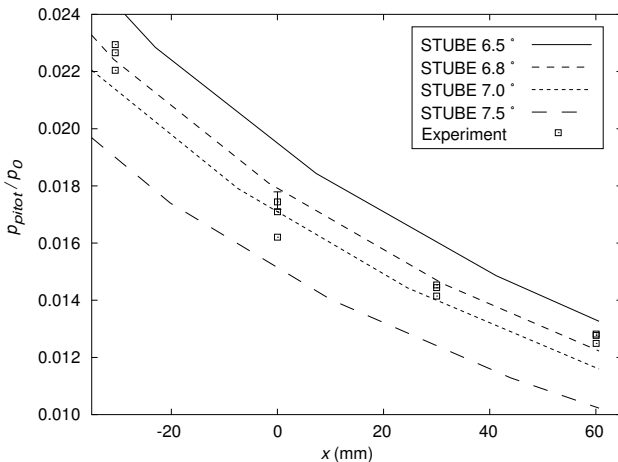


Fig. 2 Comparison of measured and calculated pitot pressures.

oxygen was added because the reactions in the reservoir cause approximately 1% NO to be formed in the reservoir and this chemical composition freezes in the nozzle, as shown in Table 1. The NO is sufficient to provide a good fluorescence signal. Nitrogen was chosen, rather than air, to provide a simpler flow that was not as strongly effected by the dissociation of O₂ as an air flow at this stagnation enthalpy.

The uncertainties in Table 1 were estimated based upon the uncertainties in the nozzle expansion angle, the measured shock speed and the nozzle-reservoir pressure. Calculations were performed at ± 1 standard deviation of these properties, and the propagation of the uncertainty through the calculation was used to estimate the uncertainty in nozzle-exit properties.

Flowfield Uniformity

The previous measurements of Palma et al.¹⁹ in this facility showed evidence of nonuniformity in one-third of PLIF images. This nonuniformity manifests as relatively large low-signal regions in the flow. That study concluded that the nonuniformity was caused by driver gas contamination of the flowfield. This was a cause for concern, as the measurements were obtained well before driver gas contamination was expected to occur. The thermometry technique used in this study requires run-to-run flow repeatability and a uniform test gas flow, so it was important to make the flow as reproducible as possible. A series of PLIF imaging experiments was performed to achieve this. Images of the freestream were obtained and parameters that might affect the flowfield uniformity were varied in sequence to see if they had an effect on the flow uniformity. The time after shock reflection at which images were obtained, the composition of the compression tube gas, the stagnation enthalpy of the flow and the test gas composition were varied, one factor at a time, but none of these had a significant effect on the flow uniformity, with similar nonuniform flows occurring to those noted in Ref. 19. An example of the nonuniform flow images

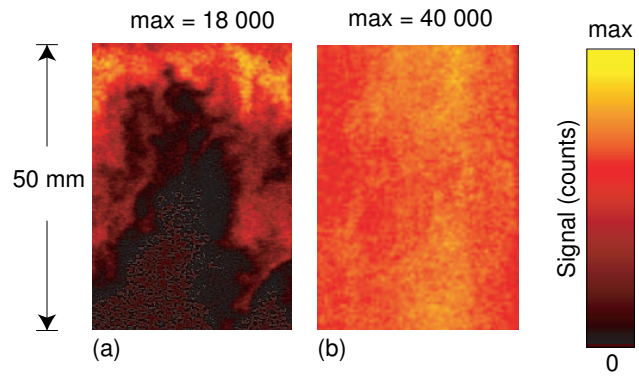


Fig. 3 PLIF images in the nozzle core flow obtained using the $^3P_{12}$ transition (a) prior to and (b) after nozzle modifications. Maximum intensity is measured in camera counts.

is shown in Fig. 3(a).

Upon inspection of the nozzle throat, some erosion was noted 7 mm downstream of the secondary diaphragm. A very small forward-facing step, less than 0.2 mm high, was noted at the position of this mylar diaphragm, where the nozzle begins to diverge. When the throat was bored out and care taken to ensure that there was no step at the secondary diaphragm position, the percentage of uniform images increased to 95%. Figure 3(b) is an example of the more uniform flow generated after redesign of the throat. The increase in signal with downstream distance is caused by the temperature decrease in the nozzle and the streaking in the image is a result of normalizing the image to the spatial laser intensity distribution. The improvement in signal uniformity after the redesign of the throat leads to the conclusion that the nonuniformity was caused by boundary-layer separation at the step in the throat. The separated boundary layer formed a re-circulating region that entrained cooler boundary-layer gas containing significantly less NO into the core flow. Over several tunnel runs, the re-attachment of this boundary layer caused the erosion downstream of the throat.

PLIF Considerations

Thermometry

The theory of planar laser-induced fluorescence is well known and has been considered elsewhere.^{25,26} The two-line thermometry method used in Ref. 27 was also used for these experiments. Two transitions are excited on succeeding tunnel runs using a thin sheet of laser light. The technique can be performed during a single tunnel run to obtain instantaneous measurements²⁸ but this technique requires two lasers and two imaging systems, which were not available for these measurements. Run-to-run variations in the nozzle reservoir pressure and shock speed varied by less than 1% throughout the measurements, and the nozzle flow was laminar within the core flow, so the assumption of run-to-run repeatability should be a good one.

Fill conditions	Mixture		p (kPa)	T (K)		
Test gas	1.1% O ₂ + 98.9% N ₂		150	297		
Driver gas	31.3% Ar + 68.7% He		118.6	297		
Reservoir conditions	p_0 (MPa)	T_0 (K)	H_0 (MJ kg ⁻¹)	u_s (ms ⁻¹)		
Value	28.0	3831	4.75	2270		
Uncertainty (%)	4.6	2.8	2.7	1.8		
Freestream conditions	p_∞ (kPa)	T_∞ (K)	u_∞ (m s ⁻¹)	ρ_∞ (kg m ⁻³)	M_∞	Re_∞ (m ⁻¹)
Nozzle exit (6.8°)	8.1	425	2850	0.064	7.03	7.9×10^6
Uncertainty (%)	7.0	5.0	2.0	5.0	2.0	5.0×10^6
Freezing species	N ₂	O ₂	NO			
Freezing temperature (K)	2030	1277	606			
Mole fractions	N ₂	O ₂	N	O	NO	Ar
Nozzle reservoir	0.9818	0.0019	0.0001	0.0034	0.0127	0.0001
Freestream	0.9835	0.0036	0.0000	0.0017	0.0111	0.0001

Table 1 T2 operating conditions for the experiment. The fill conditions, shock speed and nozzle-reservoir pressure are measured. All other quantities are calculated.

If two transitions in the same vibrational level but with differing rotational energies are excited by the laser, the rotational temperature can be determined using the relation

$$T_{rot} = \frac{(F_{J''_2} - F_{J''_1}) / k}{\ln \left(\frac{E_2 B_2 (2J''_2 + 1) Sig_1}{E_1 B_1 (2J''_1 + 1) Sig_2} \right)} \quad (4)$$

where Sig is the fluorescence signal intensity, E is the laser energy, B is the Einstein coefficient for stimulated absorption for the transition, F is the rotational energy of the transition, k is the Boltzmann constant and J'' is the rotational quantum number. The subscripts 1 and 2 refer to the two laser-excited transitions.

Analogously, if two transitions with similar rotational energies but in two different vibrational levels are excited and their fluorescence detected, the vibrational temperature can be determined from the laser energies, relative signal strengths and spectroscopic parameters using the relation

$$T_{vib} = \frac{G_{v''_2} - G_{v''_1}}{k \ln \left[\frac{E_2 B_2 Sig_1}{E_1 B_1 Sig_2} \right]} \quad (5)$$

where G is the transition vibrational energy and the other quantities are the same as those of Equation 4.

Transition Choice

Rovibronic transitions within the $A^2\Sigma^+ \leftarrow X^2\Pi$ bands (also known as the γ bands) of NO were used for the PLIF thermometry and velocimetry experiments. These bands were chosen because they gen-

erate strong fluorescence signals, they have been studied extensively and they have been shown to not have J'' -dependent quenching rates.²⁹ Four transitions were chosen within the (0,0) and (0,1) vibrational bands. Their properties are summarized in Table 2.

These transitions were carefully chosen from the large number of NO transitions available in the γ bands. Non-overlapping transitions were chosen to simplify calculations of the systematic uncertainty due to saturation of the fluorescence and absorption of the laser sheet. As shown in Table 2 the interference from surrounding transitions, ξ_{int} , is less than 0.15% for all four transitions.

Transitions with similar Einstein B coefficients were chosen to ensure that the effect of saturation was the same for both transitions. This minimized the systematic uncertainty due to saturation. As Table 2 indicates, the values of I/I_{sat} , the ratio of laser irradiance to the saturation irradiance, were made small enough to ensure that the fluorescence signal was linear with laser energy. Strong transitions such as those in the Q -branch were avoided, to minimize the effect of absorption on the measurements.

The energy difference between the transitions was made as large as possible for the rotational temperature measurements, while still providing adequate signal-to-noise at the high- J transitions. The larger the energy separation, the smaller the effect of signal uncertainty on measured temperature. A typical benchmark for desired energy separation is $\Delta F \geq kT$.²⁵ For the freestream conditions in this investigation, $\Delta F = 5.3kT$, ensuring that fluctuations

Line	v''	ν_0 (cm $^{-1}$)	F_J (cm $^{-1}$)	G_v (cm $^{-1}$)	$B_{J'J''}$ (cm J $^{-1}$)	I/I_{sat}	ξ_{int} (%)	% absorption (cm $^{-1}$)
$^O P_{12}(2.5)$	0	44 069.52	73.58	948.66	146.99	0.08	0.10	5.1
$^R R_{22}(28.5)$	0	44 483.25	1498.97	948.66	152.75	0.08	0.00	0.31
$^O P_{12}(2.5)$	1	42 193.59	73.41	2824.76	229.90	0.13	0.15	0.69
$^R R_{22}(28.5)$	1	42 622.50	1483.11	2824.76	237.93	0.13	0.00	0.04

Table 2 Spectroscopic parameters for the four thermometry transitions.

in measured signal have only a small effect on measured temperature.

The transitions in Table 2 were chosen in two pairs. Rotational temperature was measured using the $^O P_{12}(2.5)$ and the $^R R_{22}(28.5)$ transition pairs in each of the $v'' = 0$ and $v'' = 1$ vibrational levels. Two vibrational temperature measurements were made using the pair of $^O P_{12}(2.5)$ transitions in the $v'' = 0$ and $v'' = 1$ vibrational levels and using the pair of $^R R_{22}(28.5)$ transitions in the $v'' = 0$ and $v'' = 1$ vibrational levels. The symmetry of this choice of transitions enables four sets of fluorescence measurements to produce two rotational temperature maps and two vibrational temperature maps that can be directly compared with each other to check for any significant systematic error due to the choice of the rotational quantum number or vibrational level of the transitions.

Another experiment performed at these freestream conditions,²¹ obtained PLIF rotational temperature measurements using six different transitions. A Boltzmann plot indicated that the $v'' = 0$ transitions used in Table 2 produced signals consistent with a Boltzmann distribution for the NO population in that vibrational band.

PLIF System

The PLIF system used in these experiments consists of an excimer-pumped dye laser, frequency-doubled using a BBO I crystal to provide 3–5 mJ of tunable radiation between 225 and 240 nm with a spectral linewidth of 0.18 cm $^{-1}$. This system is very similar to that used in Ref. 19, but the Princeton Instruments ICCD camera used to capture the fluorescence signal has significantly better dynamic range and linearity properties than the system used in that investigation.

All the optics in the system are UV-grade fused silica. The laser sheet is formed using a combination of a cylindrical and spherical lens. In the test section, the sheet is 40-mm wide and 0.7±0.1-mm thick. Pulse-to-pulse variations in relative laser energy are measured by diverting a small portion of the beam onto a pair of quartz diffusers and then to a photodiode. A beam splitter is used to divert 8% of the sheet onto a dye cell. A CCD camera images the dye fluorescence signal, which is used to normalize the PLIF signal for spatial intensity variations across the laser sheet. Another beam splitter diverts some of the laser output

to a hydrogen/oxygen flame. The NO LIF generated in this flame is captured by a photomultiplier tube (Hamamatsu R446) at the exit of a spectrometer. An excitation scan is performed immediately before the tunnel run, to tune the laser to the center of the excitation transition.

The narrowband excitation causes fluorescence to the laser-excited band and higher vibrational bands, which is captured using a camera placed perpendicular to the laser sheet. As much of this broadband fluorescence is collected as possible, to maximize the signal. This is particularly necessary when the $v'' = 1$ vibrational level is excited, where the population is small compared to the ground vibrational state. A Schott UG5 glass filter is used to attenuate the signal from the laser-excited vibrational band, reducing the systematic error due to radiative trapping. Radiative trapping occurs when the fluorescence generated by the laser sheet excites further fluorescence in the fluid between the laser sheet and the camera. As this secondary fluorescence depends on the population in the energy state of the excited transition, different proportions of the fluorescence signal are absorbed for different transitions, leading to systematic errors in measured temperature. The UG5 filter also attenuates the influence of broadband flow luminosity caused by impurities in the flow and the elastic Mie and Rayleigh scattering from the laser.

The timing of the PLIF measurement was automated by a computer-controlled timing board, set to a delay of 350 μ s after shock reflection in the nozzle reservoir. The camera intensifier was gated for 330 ns immediately after the laser pulse, to maximize the signal-to-noise ratio.

Nine images were obtained at each transition. The camera background image and the scatter image in Fig. 5 were subtracted from each image, and the average of the images and laser energies was calculated. Equation 4 was used, with the data for rotational energy and Einstein B coefficient in Table 2, to determine the rotational temperature distributions. Vibrational temperature distributions were calculated in the same way, but using Equation 5 and the vibrational energies and B coefficients from Table 2. The camera gain was set at the same value for all of the images, so no correction for changes in camera gain was required. Spatial variations in laser irradiance were monitored using a

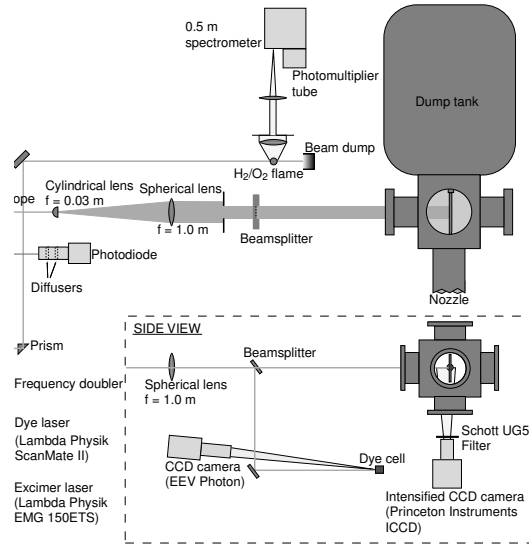


Fig. 4 Apparatus for PLIF temperature measurements.

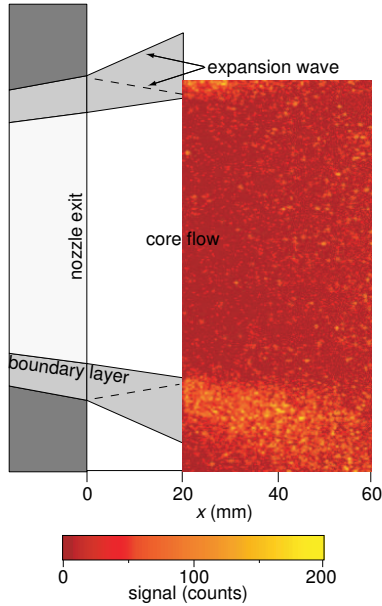


Fig. 5 Image of laser scatter, showing the position of the imaged region relative to the nozzle exit for the temperature measurements.

dye cell and the images were individually corrected for these variations before averaging.

Velocimetry

The freestream velocity was measured 29.0 ± 0.5 mm downstream of the nozzle exit, using the tagging velocimetry technique outlined in Ref. 30. This technique was chosen because it is simple, accurate and requires only a minor modification of the thermometry arrangement in Fig. 4. The 30-mm focal length cylindrical lens is replaced with a 100-mm lens rotated by 90° . This rotation allows the laser to excite a narrow line of NO molecules in the flow. The camera is delayed by 500 ns with respect to the laser. After

the gas is excited the tagged molecules advect downstream, fluorescing as they move. After the 500-ns delay, the camera is gated for 10 ns and captures the fluorescence from the excited gas. The displacement of the advected gas can be measured by fitting a Gaussian to the laser line image and calculating the center of that curve. Knowing the delay between the laser firing and the gating of the intensifier allows the velocity to be calculated from the measured displacement. The imaged region extends from 8 to 24 mm below the axis of symmetry of the flow. The imaging system was limited to this length to ensure that the displacement of the tagged gas was measurable on the CCD. For a 2700 ms^{-1} velocity and a magnification of 23 pixels mm^{-1} , the tagged particles would be displaced by 31 pixels.

Two measurements of velocity were made for this experiment, using the overlapping $^Q Q_{22}(19.5)$ and $^Q Q_{11}(2.5)$ transitions at $44\ 227.7 \text{ cm}^{-1}$. These transitions were chosen because they exhibit strong fluorescence at the freestream conditions. This is important as the fluorescence lifetime at these conditions is approximately 100 ns, and after a delay of 500 ns the signal intensity has decayed to levels that are near the resolving limit of the camera system.

Immediately before the tunnel run the test section of the tunnel was filled with a low-pressure static mixture of 1% NO in N_2 and the fluorescence in the mixture was imaged. Thus, the initial location of the laser line could be measured, providing a reference position for the displacement during the tunnel run. This was important because these measurements, unlike the flat-plate boundary-layer velocity measurements in Ref. 30, did not have a surface with a no-slip boundary condition that could act as a zero-displacement reference. Those previous measurements showed an average systematic error of 0.43 pixels displacement between the dump tank images and the images in the shock tunnel, caused by movement of the model and imaging system during them experiment. This implies an average systematic error of -50 ms^{-1} in the measured velocity.

Results

Temperature

Signal intensities in the raw images varied from approximately 500 counts above background for the $^R R_{22}(28.5)$ $v'' = 1$ transition to 30 000 counts for the $^O P_{12}(2.5)$ $v'' = 0$ transition, for a camera with a dynamic range of 65 535 counts. The maximum signal level was well below the measured linear dynamic range of the camera. The standard deviations in the signals at each of the four transitions were 13% for the $^O P_{12}(2.5)$ $v'' = 0$, 20% for the $^R R_{22}(28.5)$ $v'' = 0$ transition and 25% for the two $v'' = 1$ transitions. Similar measurements before the nozzle modifications mentioned previously had standard deviations of 23% for

the ${}^0P_{12}(2.5)$ transition, showing a considerable decrease in the uncertainty after the nozzle modification. The standard deviation for the ${}^0P_{12}(2.5)$ transition was the same as that observed in PLIF temperature measurements in a static test cell.²¹ This indicates that the measurement uncertainty is dominated by the laser and imaging systems, particularly the effect of mode competition in the laser on the spectral overlap between the laser and the transition.

The calculated uncertainty in the rotational temperature for a single pixel measurement was ± 8 K (2%) using the $v'' = 0$ transitions and ± 17 K (4%) using the $v'' = 1$ transition pair. Comparison with the 4% uncertainties quoted in the experiments of Palma et al.¹⁹ shows that the improved camera system and more uniform nozzle flow have halved the uncertainty.

Temperature maps obtained using the four transition pairs are presented in Fig. 6. The upper two images show the rotational temperature distributions while the lower two images show the measured vibrational temperature. As expected, the best signal-to-noise ratio in the rotational temperature was obtained using the two (0,0) band transitions; for the vibrational temperature, the two ${}^0P_{12}(2.5)$ transitions had the least uncertainty because the signal levels for these transitions were higher than for the ${}^R R_{22}(28.5)$ transitions.

As the flow features are clearest in the top left image for rotational temperature using the ${}^0P_{12}(2.5)$ and ${}^R R_{22}(28.5)$ $v'' = 0$ transitions, we will discuss them first. The dark region at the bottom of the image indicates the area of the test section outside the nozzle flow. In this region, the signal intensity was not sufficient to make reliable temperature measurements. At the left of the image, near $r = 30$ mm on either side of the center line, there is a region of elevated temperature, caused by the nozzle boundary layer. This temperature increase decays with axial distance from the nozzle exit as the expansion from the nozzle exit cools the flow that was in the nozzle boundary layer. There also seems to be a slight decrease in rotational temperature toward the symmetry axis of the nozzle. This is most likely caused by a reflected pattern of weak shocks and expansion waves that can form within a conical nozzle. The rotational temperature clearly decreases with axial distance from the nozzle exit, as expected of an expanding nozzle flow. The $v'' = 1$ temperature map is similar, except that the temperature increase at the nozzle boundary layer is not apparent and the signal-to-noise ratio is generally worse. The two vibrational temperature maps in the lower half of Fig. 6 show a constant vibrational temperature consistent with vibrationally frozen flow.

A clearer understanding of the radial rotational temperature distributions can be seen in the line plot of Fig. 7. This plot is of the signal in the top two rotational temperature images of Fig. 6, averaged over a

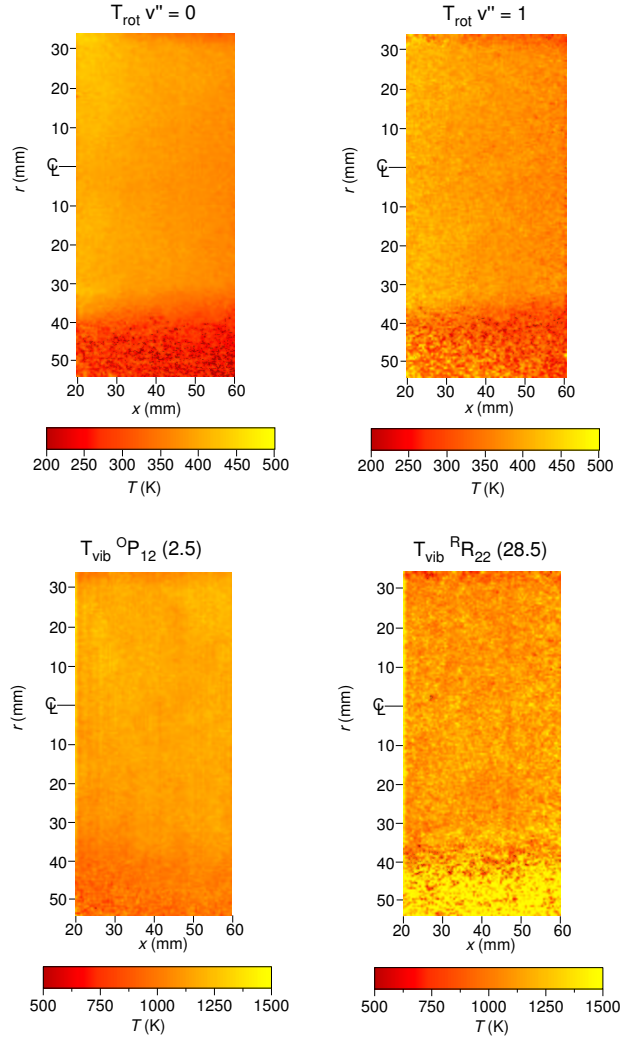


Fig. 6 Rotational and vibrational temperature maps obtained using the four transitions in Table 2.

20-mm region in the center of the temperature map. This allows a direct comparison of the two measurements made by exciting transitions in different vibrational levels.

The two radial profiles coincide between $r = 30$ mm, where the laser enters the flow, and $r = 0$ mm. Thereafter, the $v'' = 0$ rotational temperature shows a systematic increase while the temperature distribution for the $v'' = 1$ measurement is more symmetrical. This difference is caused by beam absorption in the ${}^0P_{12}(2.5)$ $v'' = 0$ PLIF image. The population in this state is much larger than for any of the other transitions and causes a measurable systematic error in the temperature for $r < 0$ mm, as a much greater proportion of the laser-sheet energy is absorbed by this transition than for the other three transitions. As Table 2 shows, the fluorescence from the ${}^R R_{22}(2.5)$ $v'' = 0$ transition absorbs 5% of the laser energy per centimeter, while the absorption of the energy for the other transitions is negligible. Further support to the

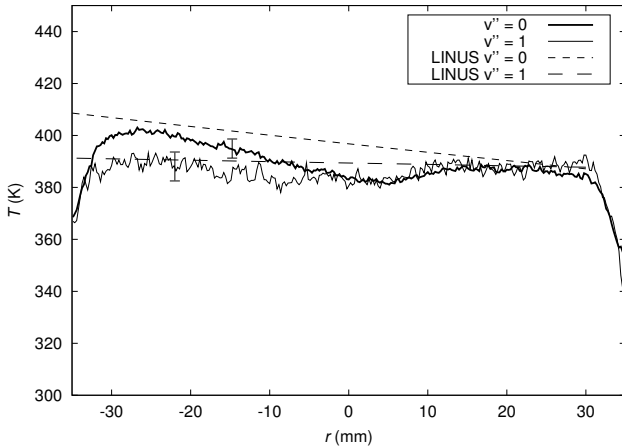


Fig. 7 Line plot of rotational temperature radial distributions for the $v'' = 0$ and $v'' = 1$ measurements, 40-mm downstream of the nozzle exit. Dashed lines indicate calculations of systematic error calculated by the LINUS program.

reasoning that the temperature difference is due to absorption can be seen from the dashed lines in Fig. 7. These lines represent calculations of the systematic error due to absorption based upon the assumption that the temperature is a uniform 390 K across the nozzle. These calculations were performed using the LINUS NO laser-induced fluorescence modeling code of Dr. P.C. Palma.³¹ Temperature distributions were calculated using the two transition pairs used to measure the two experimental distributions. The calculated temperature distributions show very similar trends to the experimental distributions, with an obvious systematic error in the $v'' = 0$ temperature distribution.

Figure 8 shows a comparison between the axial distribution of rotational temperature obtained using the $v'' = 0$ and the $v'' = 1$ transition pairs. The measurements were averaged over a 5-mm region centered at the axis. The rotational temperature distribution computed using the STUBE nozzle code for the conditions in Table 1 is included as the dashed line. The two measured temperature distributions agree to within the quoted uncertainty, both in terms of the measured temperature and the variation with axial distance. The rotational temperature decreases from 405 K at 20 mm from the nozzle exit to 360 K at 60 mm from the nozzle exit. The fact that the two temperature measurements are in agreement is an indirect indication that the rotational energy states obey a Boltzmann distribution. The agreement with the rotational temperature calculated using STUBE is also good. The STUBE result agrees both in the absolute temperature and the temperature gradient when the average shock speed is used to calculate the freestream conditions.

Despite this good agreement, it should be noted that Ref. 31 measured attenuation in shock speed of 6%

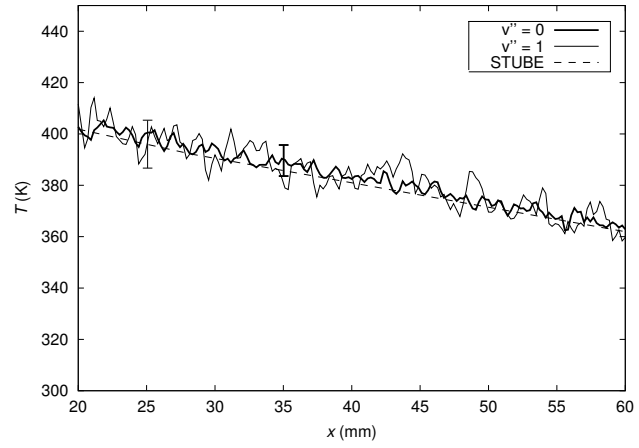


Fig. 8 Axial rotational temperature distribution for the $v'' = 0$ and $v'' = 1$ transition pairs, with the STUBE predicted distribution.

by adding a third pressure transducer to the shock tube. Using this attenuated speed would reduce the calculated freestream temperature by 35 K, so the agreement in that case would not be as good as that shown in Fig. 8. An unsteady simulation of the shock tunnel operation, accounting for the changing shock speed, would be required to more accurately simulate the effect of shock speed attenuation on the reservoir conditions.

The vibrational temperature images in Fig. 6 show constant temperatures in both the radial and axial directions. The axial vibrational temperature distributions are presented in Fig. 9. As for the rotational temperature plots, the vibrational temperature is averaged over a 5-mm region centered at the nozzle axis. The thicker solid line indicates temperature calculated using the ${}^0P_{12}(2.5)$ $v'' = 0$ and ${}^0P_{12}(2.5)$ $v'' = 1$ transition pair and the thinner line corresponds to the temperature calculated using the ${}^R R_{22}(28.5)$ $v'' = 0$ and ${}^R R_{22}(28.5)$ $v'' = 1$ line pair. The average measured NO vibrational temperature is 1162 ± 40 K for the $v'' = 0$ line pair and 1145 ± 60 K for the $v'' = 1$ pair. As for the rotational temperature measurements, the two vibrational temperature measurements agree with each other to within the measurement uncertainty. Unlike the rotational temperature distribution, the vibrational temperature is constant in the direction of flow. This indicates vibrationally frozen flow. The results of Ref. 19 show similar vibrationally frozen behavior at slightly different freestream conditions in the same facility.

The STUBE NO vibrational temperature calculation disagrees with both experimental temperature measurements by a factor of two. The most likely cause of this disagreement, also found in the vibrational temperature measurements of Ref. 19, is the modeling of the V-T interactions, as described previously. Apart from the fact that STUBE does not

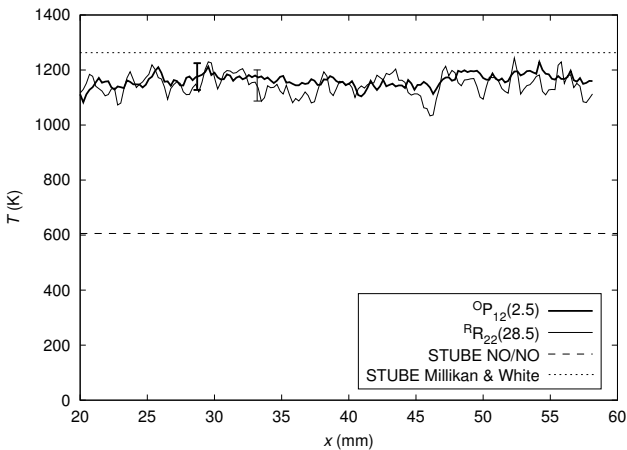


Fig. 9 Axial vibrational temperature profiles.

model V-V interactions at all, the modeling of the V-T interactions of NO assumes that the Landau-Teller rate constant for NO-N₂ collisions is the same as the measured NO-NO collision rates. This assumption is a poor one. According to Ref. 2, the relaxation rates for NO-NO collisions are much faster than that for NO-N₂ vibrational relaxation. This would have the effect of underestimating the vibrational freezing temperature as indicated in Fig. 9. Using a relaxation rate calculated using Millikan and White's empirical relation, the vibrational freezing temperature increases to 1280 K, which is much closer to the measured vibrational temperature although still outside the measurement uncertainty. If a sensible check of the vibrational temperature measurements presented in Fig. 9 is to be made, the calculation needs to account for both V-V and V-T interactions.

The large difference in the measured vibrational temperature of NO apparent in Fig. 9 has relatively little effect on the calculated rotational temperature and velocity, because NO makes up such a small proportion of the flow. Using STUBE, the difference between the calculated freestream rotational temperature assuming vibrational NO temperatures of 1280 K and 606 K was determined to be 1 K. The difference in velocity was also negligible, less than 1 ms⁻¹. This would not be the case if there was a significant systematic error in the calculated vibrational temperature of N₂, as this is the majority species in the freestream. The N₂ vibrational temperature could not be measured using the PLIF techniques described in this paper, but the CARS technique has been used to measure it in the freestream of the T3 facility.⁹ Those experiments produced N₂ vibrational temperatures consistent with the STUBE predictions.

Velocity

The two velocity measurements across the nozzle are shown in Fig. 10, with the STUBE calculated value of 2860 ± 60 ms⁻¹ shown as a dashed line. The two im-

ages produce average freestream velocities of 2660 and 2870 ms⁻¹ respectively. Given the limited number of measurements, it is difficult to be sure whether one of the measurements is an outlier. Predicted uncertainties due to jitter in the time between the laser firing and the camera gate opening (± 20 ms⁻¹), displacement measurement uncertainty (± 50 ms⁻¹) and lack of a zero-displacement reference mentioned previously are insufficient to explain the difference between the two measurements. A reasonable estimate of the freestream velocity and its uncertainty is 2750 ± 150 ms⁻¹. The measurement agrees within uncertainty with the freestream velocity of 2860 ± 60 ms⁻¹. The measured velocity distributions also show that the flow is uniform across the nozzle core, with the axial variations consistent with the measurement uncertainty.

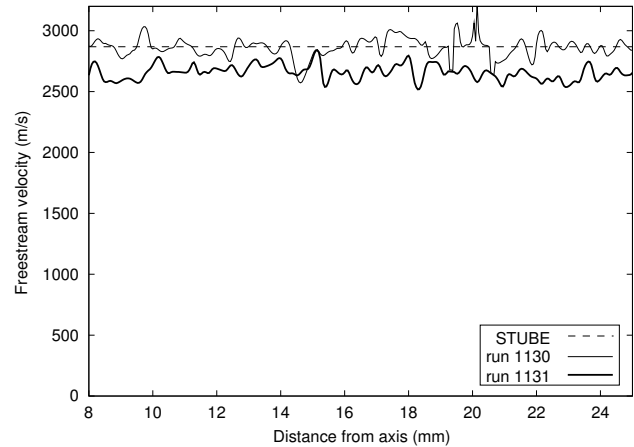


Fig. 10 Freestream velocity maps for two tunnel runs, with the STUBE calculation result.

The 5.5% velocity uncertainty is larger than the previous flat-plate measurements using the same technique³⁰ that quoted uncertainties of 2.4%. However, it should be noted that this measurement is a significant improvement on previous measurements of freestream velocity in these facilities,³² where freestream velocities were measured at high enthalpies using spark-tracer and magnetohydrodynamic techniques with an uncertainty of $\pm 17\%$. The use of zero-velocity reference, for example using a flat plate, would significantly decrease the uncertainty in this measurement.

Conclusions

Planar laser-induced fluorescence has been used to characterize the flow in a hypersonic conical nozzle, providing precise measurements of rotational temperature, NO vibrational temperature and velocity. PLIF flow visualization experiments have been used to significantly improve the uniformity of the nozzle flow, leading to a measurable increase in accuracy for the temperature measurements over previous investigations. The fact that previous studies measuring static pressure, pitot pressure, interferometry and shadow-

graph imaging did not detect this nonuniformity is a strong argument for the usefulness of PLIF imaging in these facilities.

Both vibrational and rotational measurements were consistent between two pairs of transitions, behavior that is consistent with at least the two lowest vibrational levels of NO following a Boltzmann distribution. All of the measured flow properties proved to be consistent with a simple one-dimensional nozzle code that has been used to estimate freestream conditions in a number of previous experiments. This enhances confidence in the accuracy of computed nozzle-exit conditions.

Acknowledgments

The authors wish to thank Mr. Paul Walsh for his valuable technical assistance with the shock tunnel equipment. They also thank Dr. Philip Palma for providing his LINUS code for calculations and for his valuable contributions to discussions of the PLIF technique.

References

- ¹Bray, K. N. C., "Chemical and Vibrational Nonequilibrium in Nozzle Flows," *Gasdynamics: A Series of Monographs*, Marcel Dekker, Inc, New York, 1969, pp. 59–155.
- ²Park, C., *Nonequilibrium Hypersonic Aerothermodynamics*, John Wiley and Sons, 1st ed., 1990.
- ³Vincenti, W. G. and Kruger, C. H., *Introduction to Physical Gas Dynamics*, Wiley, 1st ed., 1965.
- ⁴Millikan, R. C. and White, D. R., "Systematics of Vibrational Relaxation," *Journal of Chemical Physics*, Vol. 39, No. 12, 1963, pp. 3209–3213.
- ⁵Blackman, V. H., "Vibrational Relaxation in Oxygen and Nitrogen," *Journal of Fluid Mechanics*, Vol. 1, No. 1, 1956, pp. 61–85.
- ⁶Gillespie, W. D. and Sharma, S. P., "Raman Scattering Measurements of Vibrational Relaxation in Expanding Nitrogen," *19th International Symposium on Shock Waves*, Marseille, France, 1993, pp. 229–234.
- ⁷Del Vecchio, A., Palumbo, G., Koch, U., and Gühan, A., "Temperature Measurements by Laser-Induced Fluorescence Spectroscopy in Nonequilibrium High-Enthalpy Flow," *Journal of Thermophysics and Heat Transfer*, Vol. 14, No. 2, April 2000, pp. 216–224.
- ⁸Pilverdier, H., Brun, R., and Dumitrescu, M. P., "Emission and Raman Spectroscopy Measurements in Hypersonic Nitrogen Flows," *Journal of Thermophysics and Heat Transfer*, Vol. 15, No. 4, October–December 2001, pp. 484–490.
- ⁹Fraval, E., Danehy, P. M., and Houwing, A. F. P., "Single-shot Broadband Coherent Anti-Stokes Raman Scattering Measurements in a Free Piston Shock Tunnel Expansion," *23rd International Symposium on Shock Waves*, Fort Worth, Texas, 2001.
- ¹⁰Hurle, I. R., "Nonequilibrium Flows with Special Reference to the Nozzle-Flow Problem," *Proc. 8th International Shock Tube Symposium*, London, England, 1971.
- ¹¹Joly, V. and Marmignon, C., "Effect of H₂O Vapor on the Vibrational Relaxation in Hypersonic Wind Tunnels," *AIAA Paper 96-1855*, 1996.
- ¹²Fisher, E. R. and Smith, G. K., "Vibrational Relaxation by Metal Atoms," *Chemical Physics Letters*, Vol. 6, No. 5, 1970, pp. 438–440.
- ¹³Houwing, A. F. P., Palmer, J. L., Thurber, M. C., Wehe, S. D., Hanson, R. K., and Boyce, R. R., "Comparison of Planar Fluorescence Measurements and Computational Modelling of Shock-Layer Flow," *AIAA Journal*, Vol. 34, No. 3, 1996b, pp. 470–477.
- ¹⁴Palmer, J. L., McC Millin, B. K., and Hanson, R. K., "Multi-Line Fluorescence Imaging of the Rotational Temperature Field in a Shock Tunnel Free Jet," *Applied Physics B*, Vol. 63, No. 2, 1996, pp. 167–178.
- ¹⁵McC Millin, B. K., Palmer, J. L., and Hanson, R. K., "Temporally-Resolved, Two-Line Fluorescence Imaging of NO Temperature in a Transverse Jet in a Supersonic Crossflow," *Applied Optics*, Vol. 32, 1993, pp. 7532–7545.
- ¹⁶Danehy, P. M., Mere, P., Gaston, M. J., O'Byrne, S., Palma, P. C., and Houwing, A. F. P., "Fluorescence Measurement of the Velocity-Field Produced by the Hypersonic Separated Flow over a Cone," *AIAA Journal*, Vol. 39, No. 7, 2001b, 1320–1328.
- ¹⁷Hiller, B. and Hanson, R. K., "Simultaneous Planar Measurements of Velocity and Pressure Fields in Gas Flows Using Laser-Induced Fluorescence," *Applied Optics*, Vol. 27, No. 1, 1988, pp. 33–48.
- ¹⁸Palmer, J. L. and Hanson, R. K., "Planar Laser-induced Fluorescence Imaging in Free-jet Flows with Vibrational Nonequilibrium," *AIAA Paper 93-0046*, 1993.
- ¹⁹Palma, P. C., Danehy, P. M., and Houwing, A. F. P., "Fluorescence Imaging of Rotational and Vibrational Temperature in a Shock Tunnel Nozzle Flow," *AIAA Journal*, 2002, Submitted For Publication.
- ²⁰Stalker, R. J., "A Study of the Free-Piston Shock Tunnel," *AIAA Journal*, Vol. 5, No. 12, May 1967, pp. 2160–2165.
- ²¹O'Byrne, S., *Hypersonic Boundary Layers and Near-wake Flows*, Ph.D. thesis, Australian National University, 2002.
- ²²Gaydon, A. G. and Hurle, I. R., *The Shock Tube in High-Temperature Chemical Physics*, Chapman and Hall, 1st ed., 1963.
- ²³McC Intosh, M. K., "Computer Program for the Numerical Calculation of Frozen Equilibrium Conditions in Shock Tunnels," Tech. rep., Australian National University, 1968.
- ²⁴Vardavas, I., "Modelling Reactive Gas Flows Within Shock Tunnels," *Australian Journal of Physics*, Vol. 37, 1984, pp. 157–177.
- ²⁵Seitzman, J. M. and Hanson, R. K., "Planar Fluorescence Imaging in Gases," *Instrumentation for Flows with Combustion*, Academic Press Ltd, 1993.
- ²⁶Eckbreth, A. C., *Laser Diagnostics for Combustion, Temperature and Species*, Gordon and Breach, 2nd ed., 1996.
- ²⁷Palma, P. C., Danehy, P. M., Houwing, A. F. P., and Olejniczak, J., "PLIF Thermometry of a Free-Piston Shock-Tunnel Nozzle Flow," *AIAA Paper 98-2703*, 1998.
- ²⁸McC Millin, B. K., *Instantaneous two-line PLIF temperature imaging of nitric oxide in supersonic mixing and combustion flowfields*, Ph.D. thesis, Stanford University, 1993.
- ²⁹McC Dermid, I. S. and Laudenslager, J. B., "Radiative Lifetimes and Electronic Quenching Rate Constants for Single-Photon-Excited Rotational Levels of NO ($A^2\Sigma^+$, $v' = 0$)," *Journal of Quantitative Spectroscopy and Radiative Transfer*, Vol. 27, 1982, pp. 483–492.
- ³⁰Danehy, P. M., O'Byrne, S., and Houwing, A. F. P., "Flow-tagging Velocimetry for Hypersonic Flows Using Fluorescence of Nitric Oxide," *AIAA Paper 2001-0302*, 2001a.
- ³¹Palma, P. C., *Laser-induced fluorescence imaging in free-piston shock tunnels*, Ph.D. thesis, Australian National University, 1998.
- ³²McC Intosh, M. K., "Free Stream Velocity Measurements in a High Enthalpy Shock Tunnel," *Physics of Fluids*, Vol. 14, No. 6, June 1971, pp. 1100–1102.